Materials Transactions, Vol. 62, No. 2 (2021) pp. 229 to 238

Improvement of Mechanical Properties by Microstructural Evolution of Biomedical Co–Cr–W–Ni Alloys with the Addition of Mn and Si

Kosuke Ueki[1,*], Soh Yanagihara[2], Kyosuke Ueda[2], Masaaki Nakai[1], Takayoshi Nakano[3] and Takayuki Narushima[2,4]

[1]*Department of Mechanical Engineering, Faculty of Science and Engineering, Kindai University, Higashiosaka 577-8502, Japan*
[2]*Department of Materials Processing, Graduate School of Engineering, Tohoku University, Sendai 980-8579, Japan*
[3]*Division of Materials Science and Engineering, Graduate School of Engineering, Osaka University, Suita 565-0871, Japan*
[4]*Research Center for Structural Materials, National Institute for Materials Science, Tsukuba 305-0047, Japan*

We investigated changes in the microstructure and mechanical properties of biomedical Co–20Cr–15W–10Ni alloys (mass%) containing 8 mass% Mn and 0–3 mass% Si due to hot forging, solution treatment, cold swaging, and static recrystallization. The η-phase (M_6X–$M_{12}X$ type cubic structure, M: metallic elements, X: C and/or N, space group: Fd-3m (227)) and CoWSi type Laves phase (C14 $MgZn_2$ type hexagonal structure, space group: P63/mmc (194)) were confirmed as precipitates in the as-cast and as-forged alloys. To the best of our knowledge, this is the first report that reveals the formation of CoWSi type Laves phase precipitates in Co–Cr–W–Ni-based alloys. The addition of Si promoted the formation of precipitates of both η-phase and CoWSi type Laves phase. The solution-treated 8Mn+(0, 1)Si-added alloys exhibited TWIP-like plastic deformation behavior with an increasing work-hardening rate during the early to middle stages of plastic deformation. This plastic deformation behavior is effective in achieving both the low yield stress and high strength required to develop a high-performance balloon-expandable stent. The 8Mn+2Si-added alloy retained the CoWSi type Laves phase even after solution treatment, such that the ductility decreased but the strength improved. Additions of Mn and Si are effective in improving the ductility and strength of the Co–Cr–W–Ni alloy, respectively. [doi:10.2320/matertrans.MT-M2020300]

(Received September 8, 2020; Accepted November 30, 2020; Published January 12, 2021)

Keywords: *cobalt–chromium–tungsten–nickel alloy, manganese addition, silicon addition, mechanical properties, precipitates, plastic deformation behavior*

1. Introduction

Biomedical Co–20Cr–15W–10Ni alloy (CCWN, L605, mass%), standardized in ASTM F90, has an excellent strength–ductility balance and corrosion resistance, such that it is widely used as a metallic material for balloon-expandable stents.[1–4] Recently, the balloon-expandable stents have required a decrease in their diameter to realize a more minimally invasive treatment for cardiovascular diseases. Developing thinner stents with thicknesses ranging from 80 to 100 μm is necessary, which is the strut thickness of practical balloon-expandable stents. In other words, the strength and ductility of the CCWN alloy must be high. In addition, from the viewpoint of ease of stent expansion, the yield stress must be maintained as low as possible. For these reasons, it is imperative to develop an alloy for next-generation stents that can achieve a relatively small diameter with mechanical properties, including a high strength, high ductility, and high work-hardening rate, like that of twinning-induced plasticity (TWIP) steels. The development of a TWIP-assisted Co–Cr alloy is an effective way to reduce the diameter of balloon-expandable stents.

Stacking fault energy (SFE) is often used as an index of the plastic deformation behavior in alloy systems characterized by the occurrence of γ (fcc)-ε (hcp) allotropic transformation. CCWN alloys have a relatively high SFE among biomedical Co–Cr based alloys; this is because it contains 10 mass% Ni, which is a γ-stabilizing element in Co-based alloys. However, the SFE of the CCWN alloy at 300 K is approximately 20 $mJ \cdot m^{-2}$, which is similar to that of the Fe–Mn–Al–Si TWIP steel known as a low-SFE alloy.[5,6] Lemy and Pineau investigated the plastic deformation behavior of Co-based alloys at room temperature. They reported that both strain-induced martensitic transformation (SIMT) and deformation twinning occurred when the SFE of the alloy was within the range of 15 to 20 $mJ \cdot m^{-2}$, and deformation twinning mainly occurred when the SFE of the alloy was within the range of 20 to 30 $mJ \cdot m^{-2}$. Both deformation twinning and dislocation slip occurred when the SFE of the alloy was within the range of 30 to 50 $mJ \cdot m^{-2}$, and only dislocation slip occurred when the SFE of the alloy was higher than 50 $mJ \cdot m^{-2}$.[7] Therefore, in the CCWN alloy, SIMT and deformation twinning are considered to simultaneously occur during plastic deformation.

We previously investigated the effects of thermomechanical treatment on the microstructural, mechanical, and corrosive properties of biomedical Co–Cr alloys.[5,8–14] In our previous studies, we found that the suppression of SIMT during plastic deformation in CCWN and Co–28Cr–6Mo (CCM, mass%) alloys contribute to improved alloy ductility.[5,11] In other words, we recognize that to further improve the mechanical properties of the CCWN alloy, we must control the alterations in the microstructural behavior during plastic deformation.

Here, we focus on the use of Mn and Si, which are also constituent elements of TWIP steel, as additives to the CCWN alloy.[6] Manganese acts as a γ-stabilizing element in Co-based alloys.[15] Previous studies suggest that the addition of Mn to the CCWN alloy increases SFE and suppresses SIMT during plastic deformation.[7,15] Therefore, improvements to the ductility are expected. In addition, the strength can be improved by adding an appropriate amount of Si.[6]

*Corresponding author, E-mail: ueki@mech.kindai.ac.jp

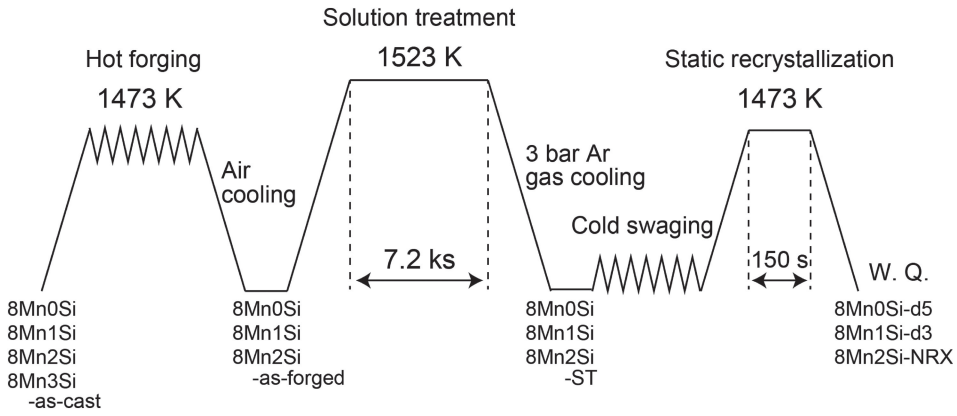

Fig. 1 Thermomechanical treatment process and the names of the specimens used in this study.

Table 1 Chemical compositions of the alloys fabricated in this study (mass%).

	Co	Cr	W	Ni	Mn	Si
8Mn0Si	Bal.	18.7	13.8	9.31	8.04	0.10
8Mn1Si	Bal.	18.5	13.7	9.22	8.06	1.03
8Mn2Si	Bal.	18.3	13.6	9.15	8.07	2.03
8Mn3Si	Bal.	18.1	13.4	9.05	8.07	3.04
L605-d207 (base alloy)	Bal.	20.1	14.9	9.77	1.58	0.07

In this study, we aim to understand the effect of Mn and Si additions on the microstructure and mechanical properties of CCWN alloys.

2. Experimental Procedures

2.1 Alloy preparation and thermomechanical treatment

Figure 1 shows the thermomechanical treatment cycle for this study. A Co–20.12Cr–14.94W–9.77Ni–1.86Fe–1.58Mn–0.079C–0.033N (mass%) alloy forged bar based on the ASTM F90 standard chemical composition (Carpenter Technology Corporation, PA, USA) was used as a base material. The base alloy is referred to as L605-d207 after the average grain size (207 μm). The base alloy, pure Mn, and pure Si were melted together using a high-frequency induction melting method. Then, the molten metals were cast into a ϕ32 mm mold and ϕ32 × 200 mm as-cast alloy rods with the chemical composition listed in Table 1 were fabricated. The alloys were referred to as 8Mn0Si, 8Mn1Si, 8Mn2Si, and 8Mn3Si. The as-cast alloys were hot forged up to ϕ22 mm at 1473 K to destroy the cast structure (as-forged alloys). The as-forged alloys were solution treated at 1523 K for 7.2 ks, which were then cooled by blowing 3 bar Ar gas over them (ST alloys). Cold swaging was performed on the ST alloys at a cross-sectional area reduction rate of 64%, and then they were machined into ϕ6.5 × 45 mm bars. The ϕ6.5 × 45 mm bar specimens were sealed inside SiO_2 ampoules with Ar gas at a pressure ranging from 0.02 to 0.03 MPa to avoid decarburization and/or denitrization of the specimen during the annealing process.[12–14] The specimens were placed into an electricity resistant muffle furnace heated to 1473 K for static recrystallization. After 150 s, the specimens were taken out from the furnace and immediately quenched by breaking the SiO_2 ampoule in iced water (recrystallized alloys).

To compare the mechanical properties of the alloy, L605-d6 alloy (average grain size = 6 μm) was also prepared by annealing the 58.3% cold swaged L605-d207 alloy at 1473 K for 100 s.[5]

2.2 Microstructure observation and analysis

The microstructures of the alloys were observed and analyzed using scanning electron microscopy in back-scattered electron mode (SEM-BSE, VE-7800, KEYENCE CORPORATION, Japan and JSM-7800F, JEOL Ltd., Japan) and electron backscatter diffraction (EBSD). The precipitates were analyzed using an electrolytic extraction method.[12–14] The metallic matrix of the alloys was electrochemically dissolved by applying a voltage of 2 V for 10.8 ks in a 10% acetylacetone–1% tetramethylammonium chloride–89% methanol (vol%) solution. The precipitates electrolytically extracted from the alloys were collected as a residue after filtering the electrolyte. The phases of the collected precipitates were identified using X-ray diffraction (XRD,

D8 advance, Bruker AXS K.K., Karlsruhe, Germany).[12–14] To more precisely identify the phases of the precipitates, crystal structure analysis via transmission electron microscopy (TEM, JEM-2100, JEOL Ltd., Japan) was also performed. The specimen for TEM analysis was prepared using a focused ion beam system (FIB, JIB-4600F, JEOL Ltd., Japan). The chemical composition of the precipitates was quantitatively analyzed using an electron probe micro-analyzer (EPMA, JXA-8530F, JEOL Ltd., Japan).

2.3 Evaluation of the mechanical properties

The mechanical properties of the ST and recrystallized alloys were evaluated by a tensile test using a mechanical tensile tester (RTF–1325, A&D Company Ltd., Tokyo, Japan). The $\phi 6.5 \times 45$ mm bar specimens were machined into the desired shapes with gauge lengths of 10 mm and diameters between gauges of 3 mm. The specimens were then pulled at a nominal strain rate of $1.67 \times 10^{-4}\,s^{-1}$ at 298 K. After the tensile test, the plastic strain was calculated by measuring the displacement of the gauge length in the fractured specimens.

3. Results

3.1 Microstructure of the as-cast and as-forged alloys

Figure 2 shows the SEM-BSE images of the as-cast alloys. Precipitates were observed in all of the as-cast alloys. The number of precipitates increased as the amount of Si increased. In the 8Mn0Si-as-cast alloy, a small number of precipitates were observed. In the 8Mn1Si-as-cast alloy, plate- and rod-shaped precipitates were observed. The plate- and rod-shaped precipitates coarsened and agglomerated in the 8Mn2Si-as-cast alloy. In the 8Mn3Si-as-cast alloy, extremely coarse precipitates with sizes ranging from 10 to 20 μm were observed. Figure 3 shows the XRD patterns of the precipitates electrolytically extracted from the as-cast alloys. The η-phase was observed in all of the as-cast alloys. The η-phase can occur as an M_6X–$M_{12}X$ type (cubic structure space group: Fd-3m (227), M: metallic elements, X: C and/or N), and the standard peak pattern of the Co_6W_6C type is shown in Fig. 3. In the 8Mn2Si and 8Mn3Si as-cast alloys, the CoWSi type Laves phase (C14 $MgZn_2$ type hexagonal structure, space group: P63/mmc (194)) was also observed in addition to the η-phase. The matrix phase of the as-cast alloys was a single γ-phase.

The 8Mn0Si, 8Mn1Si, and 8Mn2Si as-cast alloys could be hot forged up to $\phi 22$ mm without cracking, but the 8Mn3 Si as-cast alloy cracked during the hot forging process. Therefore, only 8Mn0Si, 8Mn1Si, and 8Mn2Si alloys were subjected to subsequent experiments. Figure 4 shows the SEM-BSE images of the as-forged alloys. The number of precipitates increased through hot forging of the alloys. Figure 5 shows the XRD patterns of the precipitates electrolytically extracted from the as-forged alloys. The phases observed in the precipitate of the as-forged alloys were the η-phase and CoWSi type Laves phase, which are similar to those observed in the as-cast alloys.

3.2 Microstructure and mechanical properties of ST alloys

Figure 6 shows the SEM-BSE images of the ST alloys. Precipitates of the 8Mn0Si as-forged alloy were completely dissolved by the solution treatment. In the 8Mn1Si-ST alloy, almost all precipitates were dissolved. In addition, pores formed around the remaining precipitate. These pores appear to have formed when the precipitate dissolved during solution treatment. In the 8Mn2Si-ST alloy, precipitates were observed at both the grain boundary and intragrain; the

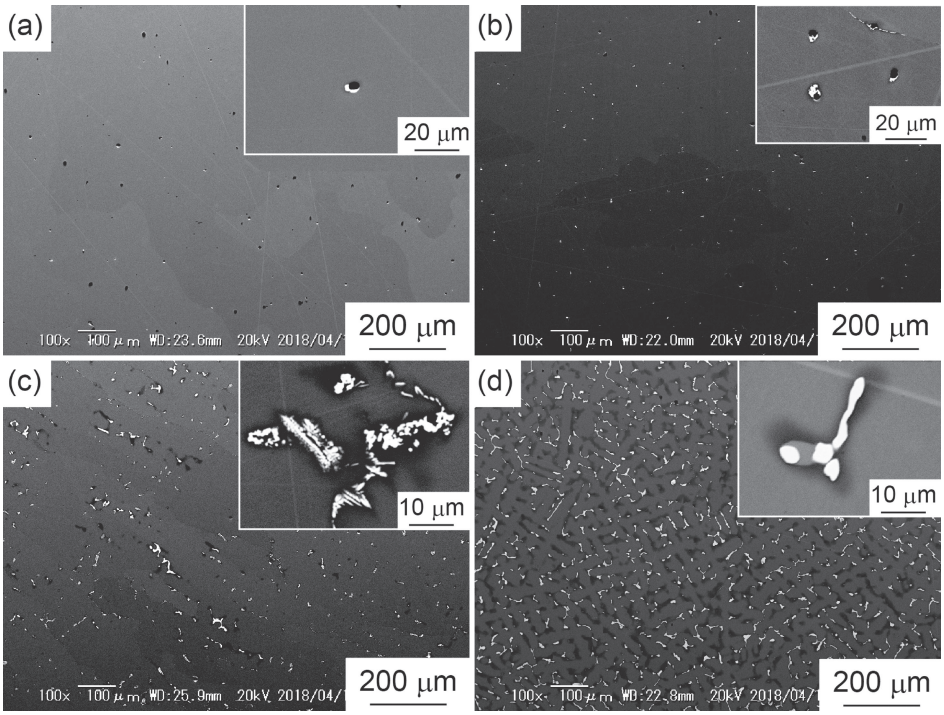

Fig. 2 SEM-BSE images of the (a) 8Mn0Si-, (b) 8Mn1Si-, (c) 8Mn2Si-, and (d) 8Mn3Si-as-cast alloys.

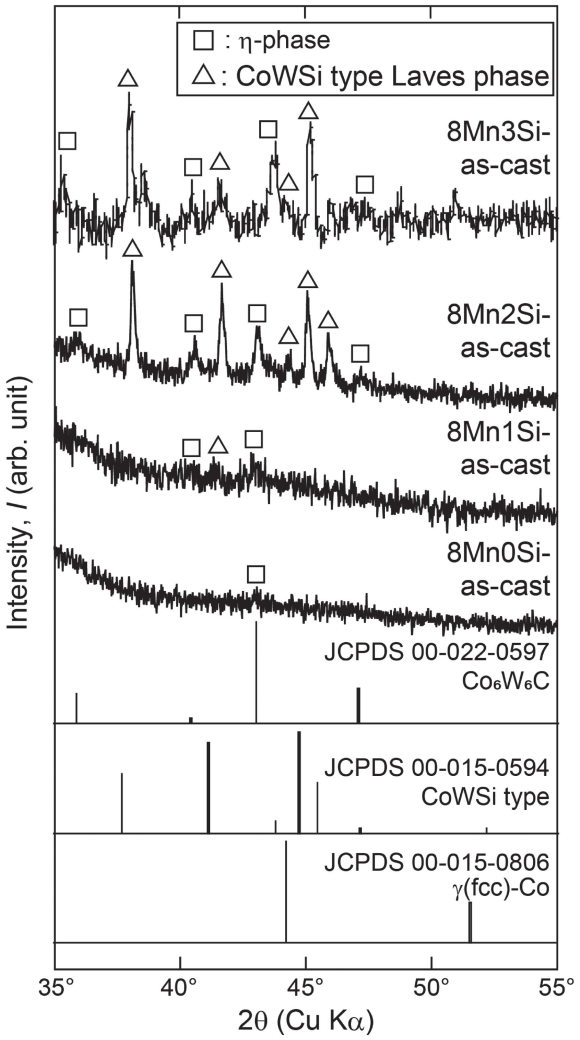

Fig. 3 XRD patterns of the precipitates electrolytically extracted from the 8Mn0Si-, 8Mn1Si-, 8Mn2Si-, and 8Mn3Si-as-cast alloys.

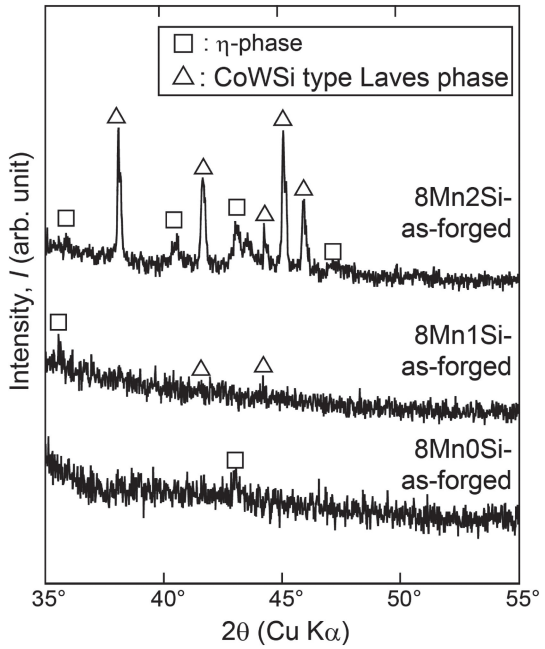

Fig. 5 XRD patterns of the precipitates electrolytically extracted from the 8Mn0Si-, 8Mn1Si-, and 8Mn2Si-as-forged alloys.

complete dissolution of the precipitates was impossible. Figure 7 shows the XRD patterns of precipitates electrolytically extracted from the ST alloys. No precipitate peaks were detected in the 8Mn0Si-ST alloy. This result is consistent with the SEM-BSE image shown in Fig. 6. Based on the results of electrolytical extraction and XRD analysis of the ST alloys, we clarified that the precipitate remaining after the solution treatment was a CoWSi type Laves phase. Figure 8 shows the TEM-bright field image and selected area diffraction pattern of the CoWSi type Laves phase observed in the 8Mn2Si-ST alloy. This result supports the

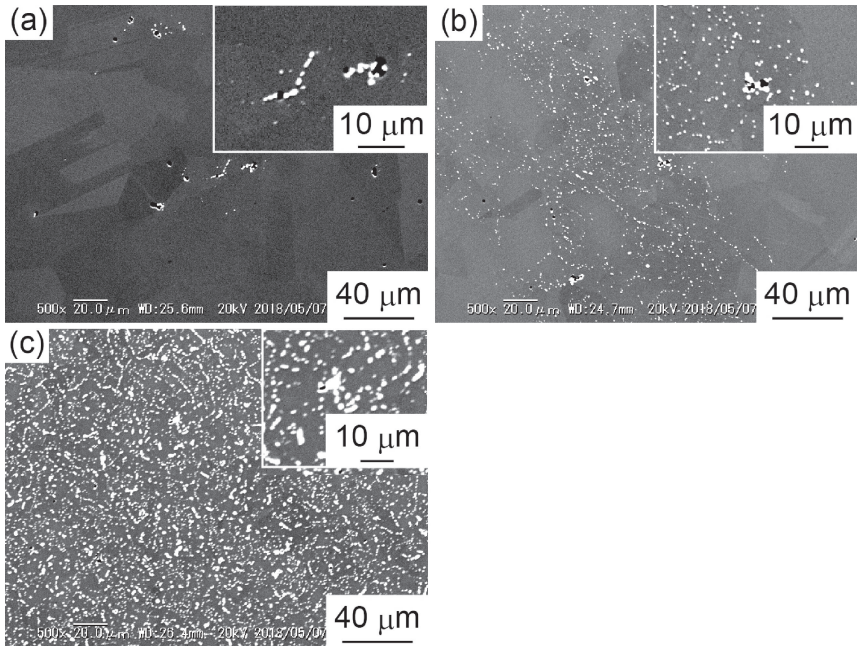

Fig. 4 SEM-BSE images of the (a) 8Mn0Si-, (b) 8Mn1Si-, and (c) 8Mn2Si-as-forged alloys.

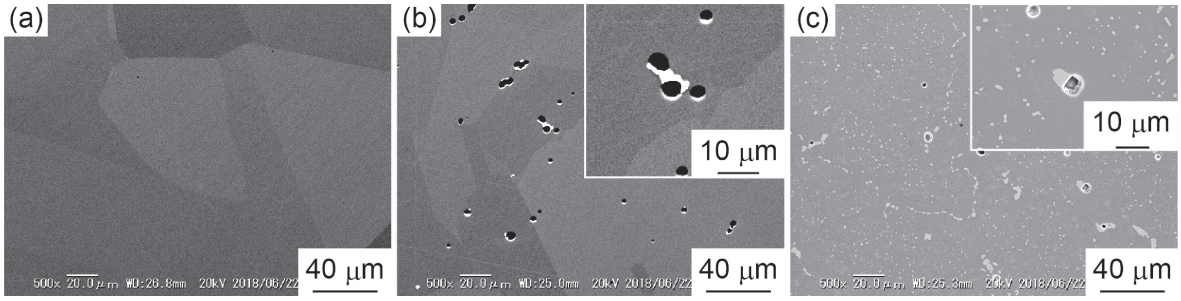

Fig. 6 SEM-BSE images of the (a) 8Mn0Si-ST, (b) 8Mn1Si-ST, and (c) 8Mn2Si-ST alloys.

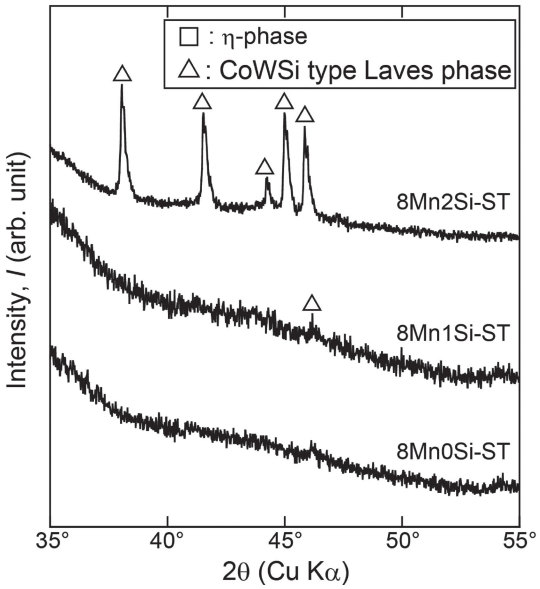

Fig. 7 XRD patterns of the precipitates electrolytically extracted from the 8Mn0Si-ST, 8Mn1Si-ST, and 8Mn2Si-ST alloys.

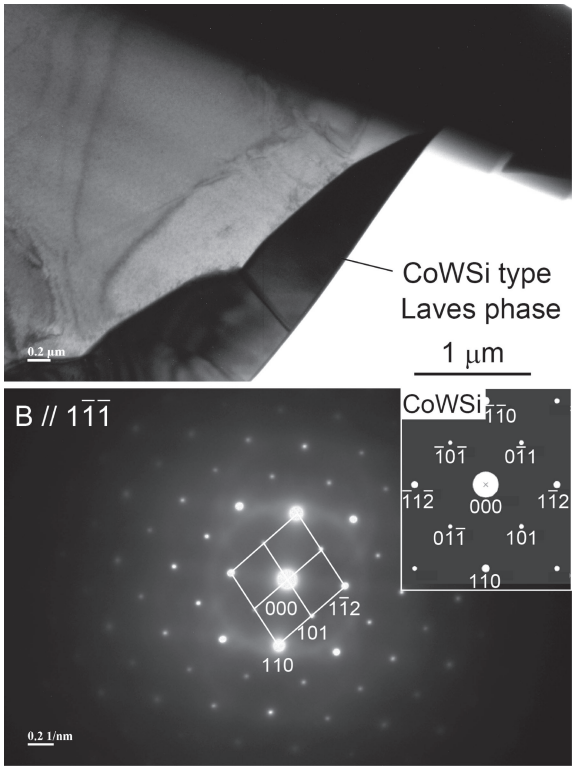

Fig. 8 TEM-BF image and SADP of the CoWSi type Laves phase observed in the 8Mn2Si-ST alloy.

idea that the precipitate confirmed in the 8Mn2Si-ST alloy was the CoWSi type Laves phase with a C14 $MgZn_2$ type structure.

Figure 9 shows the EBSD inverse pole figure (IPF) and phase maps of the 8Mn0Si-ST and 8Mn2Si-ST alloys. The average grain size calculated from the IPF maps were 129 and 133 μm for the 8Mn0Si-ST and 8Mn1Si-ST alloys, respectively. As shown in Fig. 9(a′) and (b′), the matrix of the 8Mn0Si-ST and 8Mn1Si-ST alloys has a single γ-phase.

Figure 10 shows the results of the tensile test for the 8Mn0Si-ST, 8Mn1Si-ST, and 8Mn2Si-ST alloys. To compare the mechanical properties of the alloy, Fig. 10 shows the result of the tensile test for L605-d207. The 0.2% proof stress and ultimate tensile strength of the 8Mn0Si-ST and 8Mn1Si-ST alloys were lower than that of the L605-d207 alloy. In contrast, the plastic elongation of the 8Mn0Si-ST and 8Mn1Si-ST alloys was larger than that of the L605-d207 alloy. The 8Mn2Si-ST alloy showed higher strength and lower ductility than the L605-d207 alloy.

3.3 Microstructure and mechanical properties of the recrystallized alloys

Figure 11 shows the EBSD IPF, phase, and kernel average misorientation (KAM) maps of the 8Mn0Si, 8Mn1Si, and 8Mn2Si alloys that were annealed after cold swaging. For the 8Mn0Si and 8Mn1Si alloys, a completely static recrystallized structure was obtained by annealing at 1473 K for 150 s. The average grain sizes were 5.2 and 3.1 μm for the 8Mn0Si and 8Mn1Si alloys, respectively. The 8Mn2Si alloy was not completely recrystallized. The specimens annealed at 1473 K for 150 s were referred to as 8Mn0Si-d5, 8Mn1Si-d3, and 8Mn2Si-NRX (not recrystallized) alloys based on their grain size.

Figure 12 shows the results of the tensile test for the 8Mn0Si-d5 and 8Mn1Si-d3 alloys, which was compared with that of the L605-d6 alloy. The 0.2% proof stress and ultimate tensile strength of the 8Mn0Si-d5 alloy were similar to those of the L605-d6 alloy. In contrast, the plastic elongation of the 8Mn0Si-d5 alloy was slightly higher than that of the L605-d6 alloy. The values of the 0.2% proof strength and ultimate tensile strength for the 8Mn1Si-d3 alloy were higher than those for the L605-d6 alloy, but the plastic elongation of the 8Mn1Si-d3 alloy was lower than that of the L605-d6 alloy. This was considered to be due to the presence of CoWSi type

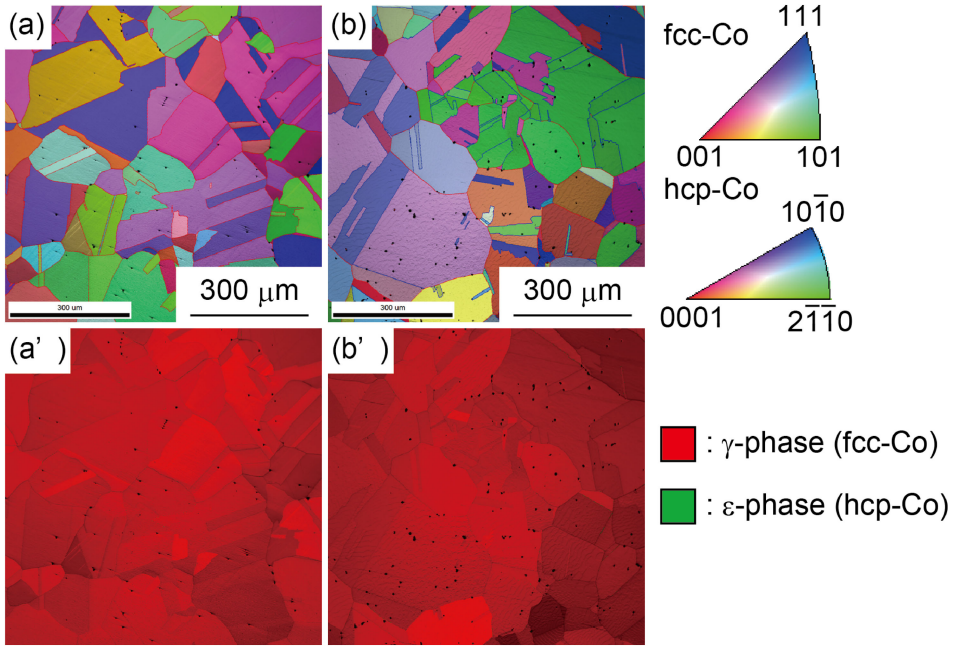

Fig. 9 EBSD IPF and phase maps of the (a), (a′) 8Mn0Si- and (b), (b′) 8Mn1Si-ST alloys.

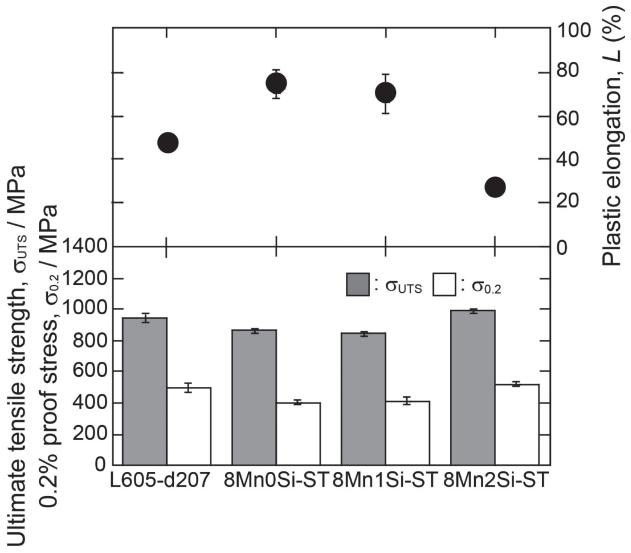

Fig. 10 Ultimate tensile strength, 0.2% proof strength, and plastic elongation of the L605-d207 alloy and ST alloys.

Laves phase and the non-uniform grain size structure in the 8Mn1Si-d3 alloy (see Fig. 11(b)).

4. Discussion

4.1 Effects of Mn and Si addition on the precipitation behavior of CCWN alloys

η-phase precipitation increases with an increase in the amount of added Si (see Figs. 3 and 5). This result is in good agreement with the results of a previous study, which stated that the addition of Si promotes the η-phase precipitation of CCM alloys.[14] In our previous study on precipitation behavior during heat treatment in the CCWN alloy, the η-phase was observed in the alloys heat treated at 1073 to 1473 K for 0.6–259.2 ks.[8,9] In addition, the amount of η-phase increased with an increasing heat treatment time.[9] Therefore, in the CCWN alloy and alloys fabricated in this study, the η-phase was a stable phase in the temperature range from 1073 to 1473 K.

In the alloy containing Si, the η-phase and CoWSi type Laves phase were observed. Li *et al.*[16] investigated the surface modification of interstitial free steel by laser cladding, reporting that the CoWSi type Laves phase formed in the surface layer when laser cladding was performed using a mixed powder of the Co–29Cr–4.5W–2Ni–1Si (mass%) alloy and SiC.[16] Yamanaka *et al.*[17] reported that a C14 type Laves phase, composed of Co, Cr, W, and Si, formed when Co–28Cr–9W–1Si–0.03C and –0.06C alloys were hot-rolled.[17] Mehrizi *et al.*[18] constructed a Gibbs free energy-composition diagram of the W–Co–Si ternary system at 298 K and reported the presence of a W–Co–Si ternary system intermetallic compound with a C14 $MgZn_2$ type hexagonal structure (space group: P63/mmc (194)), which is the same structure as the CoWSi type Laves phase detected in this study. In fact, the CoWSi type Laves phase remained in the 8Mn1Si and 8Mn2Si alloys even after the heat treatment at 1523 K for 7.2 ks. In addition, as shown in Fig. 6, the CoWSi type Laves phase formed not only at grain boundaries but also at intragrains. Therefore, when the amount of Si added was 1 to 2 mass%, the CoWSi type Laves phase is likely a stable phase. This study shows, for the first time, that the CoWSi type Laves phase can form when the alloy contains Si even if the alloy composition is close to the ASTM F90 standard; therefore, further research on the formation conditions of the CoWSi type Laves phase in Co–Cr–W–Ni type alloys is required.

The composition of the CoWSi type Laves phase was analyzed using EPMA for the 8Mn2Si-ST alloy, in which only the CoWSi type Laves phase was detected, as shown in Fig. 7. Table 2 lists the results of the EPMA quantitative analysis for the CoWSi type Laves phase observed in the

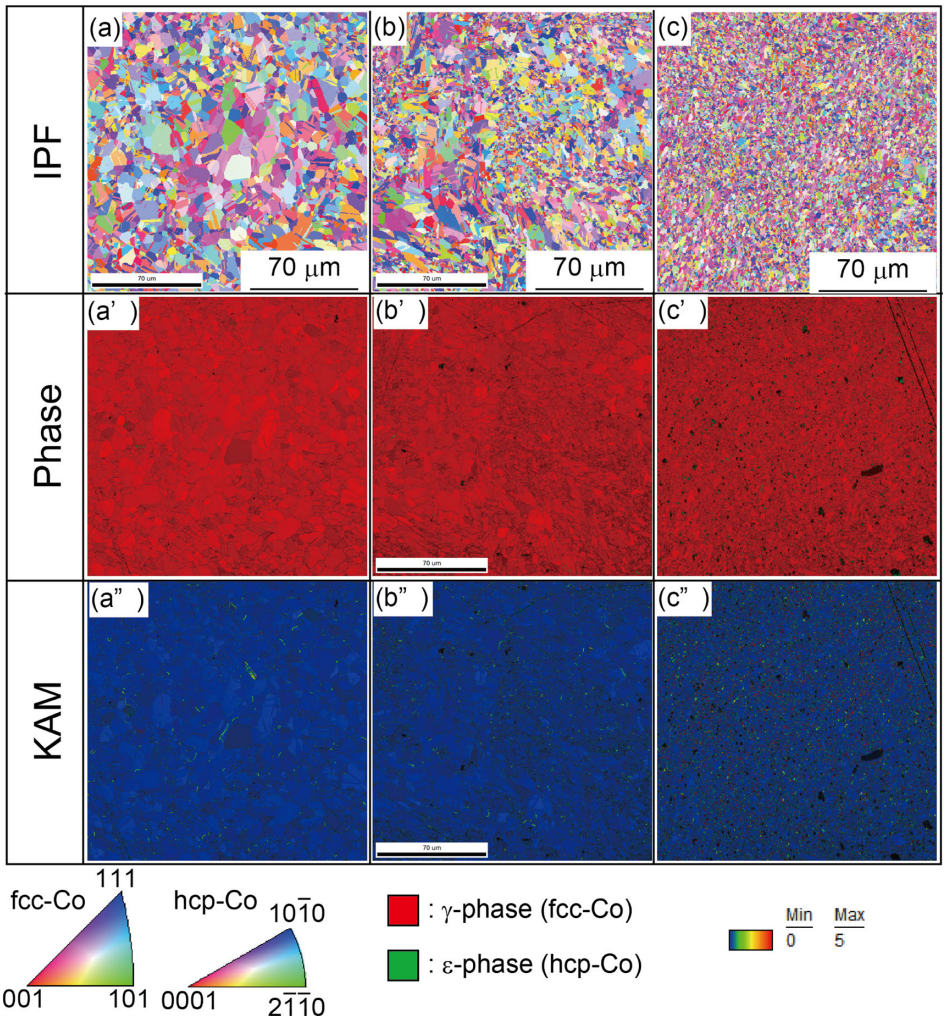

Fig. 11 EBSD IPF, phase, and KAM maps of the (a), (a′), (a″) 8Mn0Si-d5, (b), (b′), (b″) 8Mn1Si-d3, and (c), (c′), (c″) 8Mn2Si-NRX alloys.

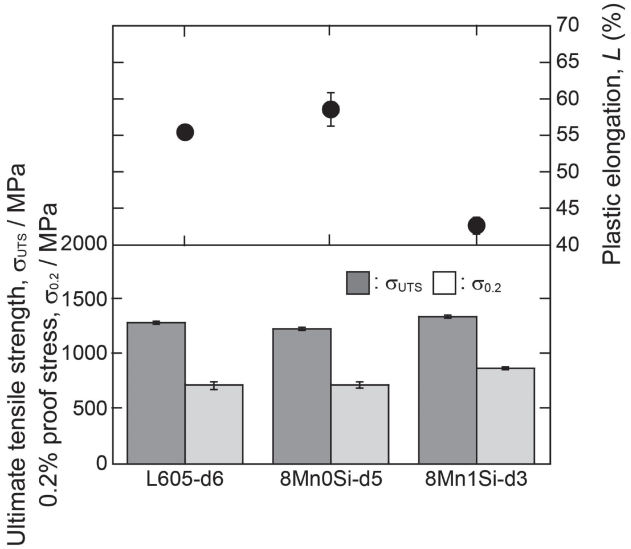

Fig. 12 Ultimate tensile strength, 0.2% proof strength, and plastic elongation of the L605-d207 and recrystallized alloys.

8Mn2Si-ST alloy. We observed that the CoWSi type Laves phase is mainly composed of Co, Cr, W, and Si, as well as a small amount of Mn, Fe, Ni, and Mo. The detection of a large amount of Si (8 mol%) indicates that Si stabilizes the CoWSi type Laves phase. The CoWSi type Laves phase confirmed in this study is likely to have a structure where W and Mo are substituted onto the Mg site and Cr, Ni, Co, and Si are substituted onto Zn sites in the C14 $MgZn_2$ type structure.[19,20] Gupta *et al.*[21,22] reported that the $Co_3Mn_3Si_2$ Laves phase and $Ni_3Mn_3Si_2$ Laves phase formed in Co–Mn–Si and Mn–Ni–Si ternary systems, respectively.[21,22] Hu *et al.*[23] showed that $Ni_3Mn_3Si_2$ formed as an equilibrium phase in the Mn–Ni–Si ternary phase diagram.[23] Furthermore, they reported that $Ni_3Mn_3Si_2$ was a C14 $MgZn_2$ type Laves phase with Mn substituted at the Mg site while Ni and Si were substituted at the Zn site.[23] In addition to the observations in these previous reports, as the atomic radius of Mn (0.161 nm)[24] is larger than that of Co, Ni, and Si (0.152, 0.149, and 0.111 nm, respectively),[24] there is a possibility that Mn could be substituted at the Mg site. Therefore, the composition of the CoWSi type Laves phase confirmed in this study can be expressed as $(W, Mo, Mn)(Cr, Fe, Co, Ni, Si)_2$.

In our previous study on the static recrystallization behavior of CCWN alloys, the average grain sizes of the CCWN alloy annealed at 1473 K for 120 s and at 1448 K for 150 s after 58.3% cold swaging were 12 and 17 μm,

Table 2 Chemical composition of the CoWSi type Laves phase analyzed by EPMA.

Co	Cr	Si	W	Fe	Ni	Mn	Mo
38.62	16.50	7.82	26.83	1.12	4.26	4.28	0.63

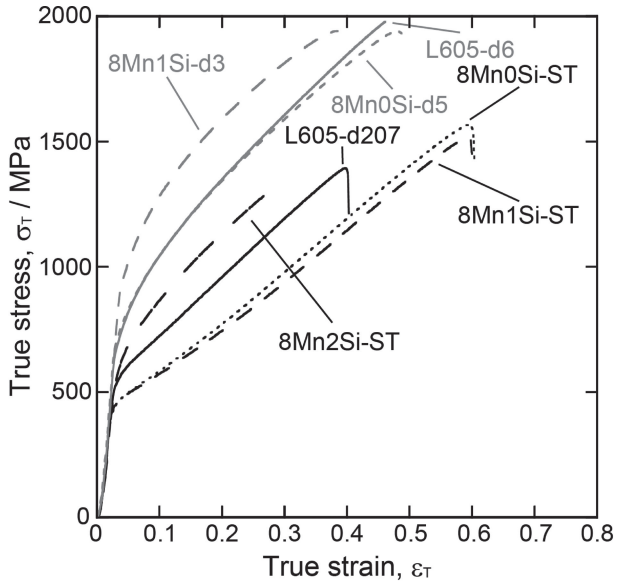

Fig. 13 True strain–true stress curves of the L605-d207, L605-d6, ST, and recrystallized alloys.

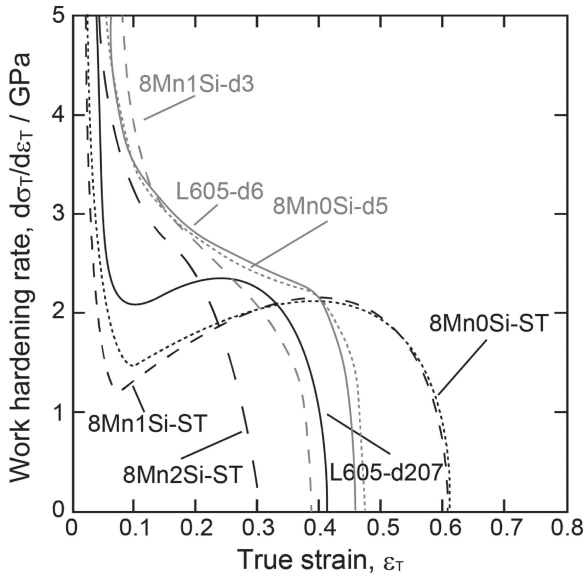

Fig. 14 Work-hardening rate curves of the L605-d207, L605-d6, ST, and recrystallized alloys.

respectively.[5] The average grain size of the recrystallized alloys in this study was significantly smaller than that of the recrystallized CCWN alloys in a previous study.[5] In the Fe–Cr–Al alloy with the addition of Nb, a previous study reported that the existence of the Fe_2Nb type Laves phase slowed the progress of static recovery and recrystallization.[25] In addition, in the 8Mn1Si and 8Mn2Si alloys, there is a possibility that the CoWSi type Laves phase hindered the progress of static recovery/recrystallization and grain growth.

4.2 Effect of the addition of Mn and Si on the plastic deformation behavior of CCWN alloys

To understand the mechanism of improvements to the ductility caused by the addition of Mn in the 8Mn0Si-ST and 8Mn1Si-ST alloys, we focused on the changes in the work-hardening behavior during plastic deformation. Figures 13 and 14 show the true stress–true strain curves and the work-hardening rate curves, respectively, of L605-d207, 8Mn0Si-ST, 8Mn1Si-ST, 8Mn0Si-ST, L605-d6, 8Mn0Si-d5, and 8Mn1Si-d3 alloys. The work-hardening rate of the 8Mn0Si-ST and 8Mn1Si-ST alloys increased from the early to middle stage of plastic deformation.

Achmad *et al.*[26] calculated the SFE of the Co–X binary system (X: Cr, W, Mo, Ni, Mn, Al, and Fe) via thermodynamic and first-principles calculations, reporting that, when 10 mol% (9.4 mass%) Mn was added to pure Co, the SFE increased by $\sim$10 mJ·m^{-2}. The effect of Si addition on the SFE of Co was calculated using Thermo-Calc (thermodynamic calculation software, database: TCFE9), revealing that the addition of 1 mass% Si to pure Co reduced the SFE by $\sim$18 mJ·m^{-2}. As the CoWSi type Laves phase was observed in the 8Mn1Si-ST alloy, we considered that the amount of Si dissolved in the matrix phase was less than 1 mass%. It is estimated that the values of SFE of the 8Mn0Si and 8Mn1Si alloys are in the range between 20 and 50 mJ·m^{-2}, in which the deformation twinning occurs.[7] Based on the SFE of the CCWN alloy,[5,7] deformation twinning may have occurred during plastic deformation in the 8Mn0Si-ST and 8Mn1Si-ST alloys; their plastic deformation behavior may be due to deformation twinning, which is similar to that of TWIP steel.[27–29]

Figure 15 shows the EBSD IPF and phase maps of the 8Mn0Si-ST alloy after a tensile test. In our previous study, we clarified that the ε-phase formed via SIMT when a strain amount of $\sim$50% is applied to a CCWN alloy. As shown in Fig. 15, almost no ε-phase formed even in the 75% strained (fractured) 8Mn0Si-ST alloy. Based on these observations, the addition of Mn to CCWN alloys appears to increase the SFE of the alloy, suppress the SIMT from the γ-phase to the ε-phase and promote deformation twinning that results in the TWIP-like work-hardening behavior. Supporting high strength, high ductility, and low-yield stress is possible by promoting the occurrence of TWIP-like work-hardening behavior. Thus, the CCWN alloy containing Mn, whose work-hardening rate increases during plastic deformation, appears to be a promising candidate for high-performance biomedical Co–Cr alloys for the development of next-generation stents with small diameters.

In the recrystallized alloys with grain sizes that are smaller than those of the ST alloys, TWIP-like work-hardening

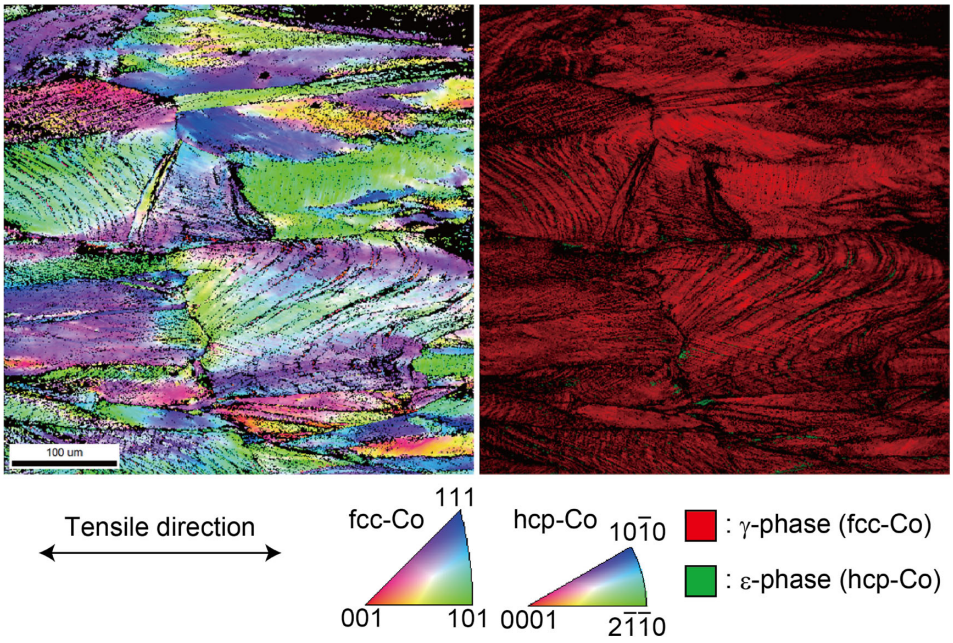

Fig. 15 EBSD IPF and phase maps of the 8Mn0Si-ST alloy after the tensile test (75% strained).

behavior was not observed, as shown in Figs. 13 and 14. The deformation twinning stress (τ_{tw}) can be expressed as follows:[30]

$$\tau_{tw} = \frac{\gamma}{b} + \frac{K_{tw}^{H-P}}{\sqrt{D}}, \quad (1)$$

where γ is the SFE, b is the Burgers vector, K_{tw}^{H-P} is the Hall–Petch constant of deformation twinning, and D is the grain size. The value of τ_{tw} increases with grain refinement, such that deformation twinning is less likely to occur with an increase in τ_{tw}. Therefore, the work-hardening rate does not increase during plastic deformation in the recrystallized alloys.

The 8Mn2Si-ST alloy shows higher strength and lower ductility than the L605-d207 alloy. Furthermore, compared with the 8Mn1Si-ST alloy, in the 8Mn2Si-ST alloy, the strength improves and the ductility decreases. This may be because of the increase in the amount of CoWSi type Laves phase that results from the increase in the amount of Si. In a previous study on Co–Cr–W–Si alloy,[17] the 0.2% proof stress and the ultimate tensile strength increased with an increase in the amount of the Laves phase owing to the addition of C. The relationship between the amount of Laves phase and strength in this study is in good agreement with the results of that study.[17]

The recrystallized alloys fabricated in this study have an average grain size ranging from 3 to 5 μm, which is relatively small when compared with the grain size of stents used for practical purposes (20–30 μm). In other words, the alloy to be used in the development of next-generation small-diameter stents should exhibit TWIP-like work-hardening behavior while maintaining high strength with a grain size of approximately 20 μm. To meet these requirements, future studies must investigate the optimization of the thermomechanical treatment conditions and the amount of Mn and Si added to the CCWN alloy.

5. Conclusion

Biomedical Co–20Cr–15W–10Ni (mass%) alloys containing Mn (8 mass%) and Si (~3 mass%) were fabricated and the effects of the Mn and Si content on their precipitation behavior, mechanical properties, and plastic deformation behavior were investigated. Based on our results, we can draw the following conclusions.

- The phases of the precipitates formed in the CCWN alloy containing Mn and Si were the η-phase and CoWSi type Laves phase. In the Co–Cr–W–Ni alloy system, the addition of Si promoted the formation of these precipitates. The formation of CoWSi type Laves phase in a Co–Cr–W–Ni alloy system was first confirmed in this study.
- The addition of Mn to the CCWN alloy improved the ductility of the alloy. The 8Mn0Si-ST alloy exhibited TWIP-like plastic deformation behavior when the work-hardening rate was increased in the early to middle stages of plastic deformation. This plastic deformation behavior was due to the increase in the SFE that resulted from the addition of Mn that promoted deformation twinning during plastic deformation. The addition of Mn to the CCWN alloy is an effective method for designing alloys with high strength, high ductility, and low yield stress.
- In the 8Mn2Si-ST alloy, the strength improved, but the ductility decreased when compared with the 8Mn0Si-ST and 8Mn1Si-ST alloys. The addition of Si to a CCWN alloy is an effective method to improve its strength.
- The 8Mn0Si-d5 alloy showed slightly high ductility with a similar level of strength as the L605-d6 alloy. The plastic elongation of the 8Mn1Si-d3 alloy was lower than that of the L605-d6 alloy because of the presence of the CoWSi type Laves phase and a non-uniform grain size structure.

Acknowledgments

This study was financially supported by the Japan Society for the Promotion of Science KAKENHI [grant numbers JP 16J04279, JP 19K23580]. We thank the Division of Joint Research Center, Kindai University, for the XRD measurements and Dr. K. Kobayashi of Tohoku University for the TEM and EPMA analyses.

REFERENCES

1) J. Favre, Y. Koizumi, A. Chiba, D. Fabregue and E. Maire: Metall. Mater. Trans. A **44** (2013) 2819–2830.
2) P. Poncin and J. Proft: Proc. Materials and Processes for Medical Devices Conference, (ASM International, 2004) pp. 253–259.
3) F.R. Morral: J. Mater. **1** (1966) 384–412.
4) R.V. Marrey, R. Butgermeister, R.B. Grishaber and R.O. Ritchie: Biomaterials **27** (2006) 1988–2000.
5) K. Ueki, S. Yanagihara, K. Ueda, M. Nakai, T. Nakano and T. Narushima: Mater. Sci. Eng. A **766** (2019) 138400.
6) D.T. Pierce, J. Bentley, J.A. Jiménez and J.E. Wittig: Scr. Mater. **66** (2012) 753–756.
7) L. Rémy and A. Pineau: Mater. Sci. Eng. **26** (1976) 123–132.
8) T. Narushima, S. Mineta, Y. Kurihara and K. Ueda: JOM **65** (2013) 489–504.
9) K. Ueki, K. Ueda and T. Narushima: Metall. Mater. Trans. A **47** (2016) 2773–2782.
10) K. Ueki, K. Ueda, M. Nakai, T. Nakano and T. Narushima: Metall. Mater. Trans. A **49** (2018) 2393–2404.
11) K. Ueki, M. Abe, K. Ueda, M. Nakai, T. Nakano and T. Narushima: Mater. Sci. Eng. A **739** (2019) 53–61.
12) S. Mineta, Alfirano, S. Namba, T. Yoneda, K. Ueda and T. Narushima: Metall. Mater. Trans. A **43** (2012) 3351–3358.
13) S. Mineta, S. Namba, T. Yoneda, T. Ueda and T. Narushima: Metall. Mater. Trans. A **41** (2010) 2129–2138.
14) Alfirano, S. Mineta, S. Namba, T. Yoneda, K. Ueda and T. Narushima: Metall. Mater. Trans. A **42** (2011) 1941–1949.
15) T.L. Achmad, W. Fu, H. Chen, C. Zhang and Z.G. Yang: Comput. Mater. Sci. **121** (2016) 86–96.
16) M.X. Li, Y.Z. He and G.X. Sun: Mater. Des. **25** (2004) 355–358.
17) K. Yamanaka, M. Mori, K. Kuramoto and A. Chiba: Mater. Des. **55** (2014) 987–998.
18) M.Z. Mehrizi and R. Beygi: J. Adv. Mater. Process. **5** (2017) 23–32.
19) K. Yamamoto, Y. Kimura and Y. Mishima: Mater. Trans. **45** (2004) 2598–2601.
20) K. Young, T. Ouchi and M.A. Fetcenko: J. Alloy. Compd. **476** (2009) 774–781.
21) K.P. Gupta: J. Phase Equilibria Diffus. **27** (2006) 517–522.
22) K.P. Gupta: J. Phase Equilibria Diffus. **27** (2006) 529–534.
23) B. Hu, H. Xu, S. Liu, Y. Du, C. He, C. Sha, D. Zhao and Y. Peng: Calphad **35** (2011) 346–354.
24) E. Clementi, D.L. Raimondi and W.P. Reinhardt: J. Chem. Phys. **38** (1963) 2686–2689.
25) Z. Sun, P.D. Edmondson and Y. Yamamoto: Acta Mater. **144** (2018) 716–727.
26) T.L. Achmad, W. Fu, H. Chen, C. Zhang and Y.G. Yang: J. Alloy. Compd. **694** (2017) 1265–1279.
27) D.T. Pierce, J.A. Jiménez, J. Bentley, D. Raabe, C. Oskay and J.E. Wittig: Acta Mater. **68** (2014) 238–253.
28) D.T. Pierce, J.A. Jiménez, J. Bentley, D. Raabe and J.E. Wittig: Acta Mater. **100** (2015) 178–190.
29) H. Ding, Z.Y. Tang, W. Li, M. Wang and D. Song: J. Iron Steel Res. Int. **13** (2006) 66–70.
30) I.G. Urrutia, S. Zaefferer and D. Raabe: Mater. Sci. Eng. A **527** (2010) 3552–3560.